Fluxon-based quantum simulation in circuit QED

Alexandru Petrescu,[1,*] Hakan E. Türeci,[1] Alexey V. Ustinov,[2,3] and Ioan M. Pop[2,4]

[1]*Department of Electrical Engineering, Princeton University, Princeton, New Jersey 08544, USA*
[2]*Physikalisches Institut, Karlsruhe Institute of Technology, 76131 Karlsruhe, Germany*
[3]*Russian Quantum Center, National University of Science and Technology MISIS, 119049 Moscow, Russia*
[4]*Institute of Nanotechnology, Karlsruhe Institute of Technology, 76344 Eggenstein Leopoldshafen, Germany*

Long-lived fluxon excitations can be trapped inside a superinductor ring, which is divided into an array of loops by a periodic sequence of Josephson junctions in the quantum regime, thereby allowing fluxons to tunnel between neighboring sites. By tuning the Josephson couplings and, implicitly, the fluxon tunneling probability amplitudes, a wide class of one-dimensional tight-binding lattice models may be implemented and populated with a stable number of fluxons. We illustrate the use of this quantum simulation platform by discussing the Su-Schrieffer-Heeger model in the one-fluxon subspace, which hosts a symmetry-protected topological phase with fractionally charged bound states at the edges. This pair of localized edge states could be used to implement a superconducting qubit increasingly decoupled from decoherence mechanisms.

I. INTRODUCTION

With recent advances in state preparation and measurement techniques, circuit quantum electrodynamics (cQED) architectures [1,2] are becoming increasingly attractive for quantum information processing and quantum simulation [3]. Other platforms for quantum simulation include ultracold atoms in traps and optical lattices [4], trapped ions [5,6], Josephson junction arrays [7], and photonic systems [8]. One of the main efforts in quantum simulation has been the implementation of interacting, strongly correlated models, which possess rich physics but are, in general, analytically intractable.

There is an increasing list of proposals based on the cQED architecture, which notably includes analogs of the seminal boson Hubbard model [9] for the superfluid-to-insulator transition of lattice bosons with repulsive contact interactions [10–17], the fermion Hubbard model [18], and topological order [19,20]. Recently, several implementations successfully showed proof-of-concept quantum simulation of dissipative phase transitions [21], molecules [22] or fermionic tight-binding models [23], and the Rabi model in the strong and ultrastrong coupling regimes [24–28], heralding studies of spin-boson and Kondo physics [29].

Microwave photons, the physical building block for cQED quantum Hamiltonians, are nevertheless subjected to intrinsic dissipation. One solution to circumvent the limitations imposed by photon loss is to stabilize quantum states using bath-engineering schemes for single qubits [30,31] or qubit arrays [32–34].

In this work, we propose an alternative way to simulate lattice models, where the ground state of the effective Hamiltonian is unaffected by photon losses. Specifically, we show how to engineer arbitrary one-dimensional tight-binding models for quantum fluxons, i.e., 2π kinks in the superconducting phase, associated with strongly confined Josephson fluxoids in a discretized extended junction with high kinetic inductance. Fluxons correspond to remarkably stable quantized persistent currents I_p flowing around superconducting loops containing Josephson junctions [Figs. 1(a)–1(c)]. In order to load a certain number of fluxons m inside the ring, one can use a protocol very similar to the one demonstrated in Ref. [35] for the reset of a superinductor loop to its ground state with $m = 0$ [Figs. 1(d) and 1(e)]. We expect this protocol to successfully implement the desired m-fluxon state with a probability in excess of 90%, stable for an extended duration of time, on the order of hours or even days [35].

In the classical regime, fluxons constitute the basis for rapid single-flux quantum electronics [36], where current biases close to the critical current prompt fluxon mobility. The associated heating is low enough to make them attractive for state-of-the-art classical information processing [37], notably in the recent design of a qubit readout circuit [38].

Fluxons obeying macroscopic quantum tunneling are significantly more fragile. Following their first implementation a decade ago [39], their use in devices has remained limited with few exceptions [40–42]. One of the main challenges in the development of quantum fluxon electronics was the absence of reliable superinductors, inductors L with an rf impedance comparable to the resistance quantum: $L\omega \geqslant R_Q = h/(2e)^2 \approx 6.5\,\text{k}\Omega$. A superinductor needs to allow for large quantum fluctuations of the phase while preventing its macroscopic quantum tunneling.

The remarkable recent progress in superinductor design and fabrication [35,43,44], including their use in artificial crystals and molecules [45–47], renders possible the physical implementation of the quantum fluxon platform proposed here. Recently, it was shown that granular aluminum

---

*Present address: Institut quantique and Département de Physique, Université de Sherbrooke, Sherbrooke J1K 2R1 QC, Canada.
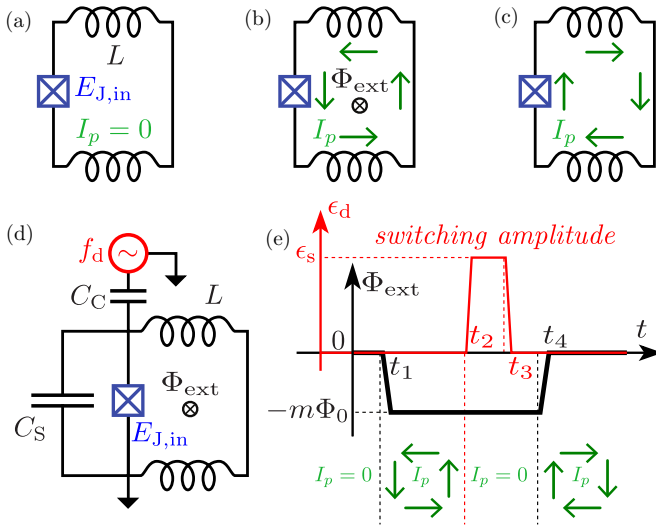
FIG. 1. Fluxon state preparation. The top row shows the three possible configurations of the superinductor loop: (a) no persistent current $I_p = 0$, (b) persistent current under external flux, and (c) m fluxons trapped inside of the loop with zero external field. (d) Circuit setup for insertion of fluxons under external flux and drive. (e) Protocol for drive amplitude $\epsilon_d(t)$ (red) and external flux $\Phi_{\text{ext}}(t)$ (black) for the insertion of m fluxons. The drive frequency $f_d \approx \frac{1}{2\pi}(L_{\text{J,in}}C_{\text{S}})^{-1/2}$ corresponds to the eigenmode of the radio-frequency resonator consisting of the input junction $E_{\text{J,in}}$ and the shunt capacitance C_{S}. The corresponding persistent currents are represented by the green arrows (see Appendix A).

wires of submicron width can implement almost perfect superinductors featuring state-of-the-art coherence and low nonlinearity [48,49].

The key insight of our proposal is to implement a tight-binding model for long-lived quantum fluxons trapped inside a superinductor ring. The ring is divided into smaller loops by a periodic sequence of quantum Josephson junctions [see Fig. 2(a)], with $E_{\text{J},i}/E_{\text{C},i}^- \lesssim 10$, where $E_{\text{J},i}$ is the Josephson coupling of the ith junction and $E_{\text{C},i}^- = e^2/[2(C_{\text{J},i} + C_0/2)]$ is the corresponding charging energy. At the classical level, thanks to the large superinductance on the surrounding ring, fluxons are confined to single loops, in contrast to the case of long Josephson junctions or isotropic Josephson junction arrays [50]. The charging energies allow fluxons to tunnel between neighboring loops, with a tunneling amplitude whose spatial dependence is modulated by the Josephson couplings. The tunnel rates can be either predefined by fabrication or tuned *in situ* using locally flux biased superconducting quantum interference device (SQUID) loops, which would also mitigate the inherent spread in junction parameters. A wide class of one-dimensional tight-binding lattice models could be implemented and populated with a stable number m of fluxons. Additionally, local fast-flux lines would enable the use of the same platform for quantum annealing [51].

The remainder of this paper is organized as follows. In Sec. II, we derive the circuit Hamiltonian and provide a definition of a fluxon trapped in the system. In Sec. III, we derive a low-energy effective theory for the dynamics of a single fluxon in terms of a tight-binding model and argue that this
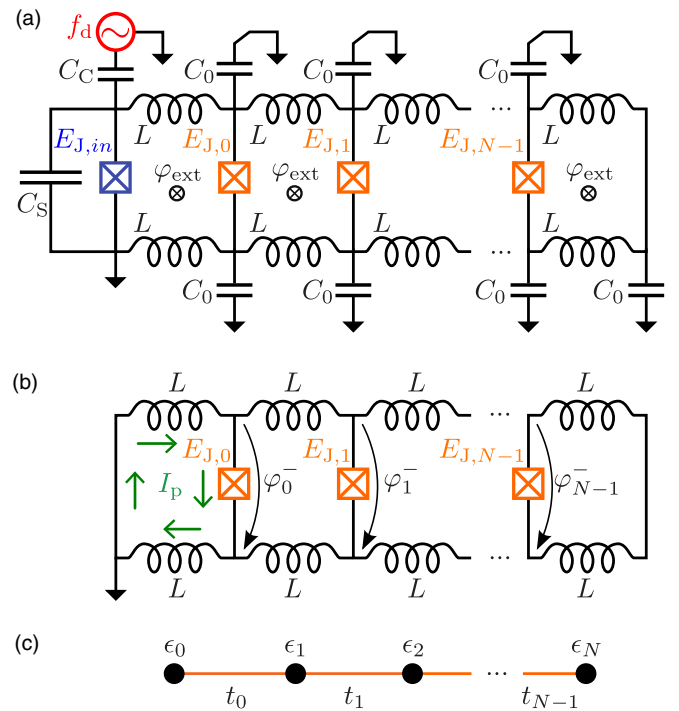

FIG. 2. Superconducting circuit implementation of an effective tight-binding model for fluxons. (a) The circuit in Fig. 1 generalizes to a superinductor ring encompassing loops separated by Josephson junctions. The fluxon "input" junction is shown in blue, the "lattice" junctions $E_{\text{J},i}$ are depicted in orange. (b) Circuit representation of the simplified model of Eq. (4); the branch fluxes φ_i^- are the degrees of freedom describing fluxon dynamics through the one-dimensional array. (c) The equivalent tight-binding model for fluxons, where every site corresponds to a loop in (b); the on-site and tunneling energy scales are the ones that appear in Eq. (8).

is indeed the correct low-energy description by numerically diagonalizing the circuit problem for small numbers of junctions. Finally, we conclude in Sec. IV. We relegate substantial detail to the Appendixes: Appendix A covers the protocol for fluxon insertion. We provide the detailed derivation of the circuit Hamiltonian in Appendix B. We dedicate Appendix C to numerical methods, and we provide a discussion of the effects of disorder in Appendix D.

II. CIRCUIT HAMILTONIAN

We now consider a simplified version of the circuit [Fig. 2(b)] in which the fluxon insertion circuitry can be neglected ($L_{\text{J,in}} \ll L$). The circuit consists of $2N$ superconducting islands denoted by indices α, i, with $i = 1, \ldots, N$ being the longitudinal coordinate and $\alpha = 1, 2$ being the transverse coordinate. The degrees of freedom are canonically conjugate pairs of superconducting phase and Cooper pair number operators on the superconducting islands, obeying $[\varphi_{\alpha,i}, n_{\beta,j}] = i\delta_{\alpha\beta}\delta_{ij}$. We introduce linear combinations corresponding to longitudinal and transverse modes,

$$\varphi_i^{\pm} = \varphi_{1,i} \pm \varphi_{2,i}, \quad n_i^{\pm} = \frac{n_{1,i} \pm n_{2,i}}{2}, \tag{1}$$

respectively, for which $[\varphi_i^\eta, n_j^{\eta'}] = i\delta_{\eta\eta'}\delta_{ij}$ for $\eta, \eta' = \pm$. The transverse variables φ_i^- and n_i^- denote the branch flux, in units of the superconducting flux quantum $\Phi_0/(2\pi)$, and Cooper pair number difference across the ith Josephson junction, respectively.

Using the notation introduced in Eq. (1), the circuit Hamiltonian separates as $\mathcal{H} = \mathcal{H}^+ + \mathcal{H}^-$ (see Appendix B for the derivation). The fluxon Hamiltonian is $\mathcal{H}^-$, while $\mathcal{H}^+$ describes the longitudinal "parasitic" modes of the transmission line in Fig. 2(a):

$$\mathcal{H}^+ = \sum_{i=0}^{N-1} 4E_C^+(n_i^+)^2 + \sum_{i=0}^{N-2} \frac{E_L}{2}(\varphi_{i+1}^+ - \varphi_i^+ - \varphi_{\text{ext},i+1})^2. \tag{2}$$

$E_C^+ = e^2/C_0$ are Coulomb charging energies, with C_0 being the capacitance to ground of each superconducting island. $E_L = [\Phi_0/(2\pi)]^2/(2L)$ are inductive energies, and $\varphi_{\text{ext},i} = 2\pi\Phi_{\text{ext},i}/\Phi_0$ is the external flux. Typical values are $C_0 \sim$ 40 aF and $L \sim 100$ nH [35]. Since there are N pairs of superconducting islands, the plasma frequency characterizing the excitations of the transmission line scales as

$$\omega^+ = \frac{1}{N\sqrt{LC_0}} \sim \frac{500}{N} \text{ GHz}. \tag{3}$$

On the other hand, the typical energy scale of the antisymmetric sector $\mathcal{H}^-$ is set by the tunneling energies t_i [see Fig. 2(c) and Eq. (8)], which are on the order of ~ 10 GHz. Given the symmetry of the circuit in Fig. 2, these sectors are orthogonal, and moreover, they are spectrally isolated ($\omega^+ \gtrsim t_i$) for $N \lesssim 50$.

Second, $\mathcal{H}^-$ describes the transverse modes [see Fig. 2(b)], which we express as

$$\mathcal{H}^- = \mathcal{T}^- + \mathcal{V}^-, \tag{4}$$

whose terms are

$$\mathcal{T}^- = \sum_{i=0}^{N-1} 4E_{C,i}^-(n_i^-)^2, \tag{5}$$

with $E_{C,i}^- = e^2/[2(C_{J,i} + C_0/2)] \simeq e^2/2C_{J,i}$ being the Coulomb charging energy between the two superconducting islands, and

$$\mathcal{V}^- = \frac{E_L}{2}(\varphi_0^- - \varphi_{\text{ext},0})^2 + \frac{E_L}{2}(\varphi_{N-1}^- + \varphi_{\text{ext},N})^2 + \sum_{i=0}^{N-2} \frac{E_L}{2}(\varphi_{i+1}^- - \varphi_i^- - \varphi_{\text{ext},i+1})^2 + \sum_{i=0}^{N-1} E_{J,i}[1 - \cos(\varphi_i^-)] \tag{6}$$

being the potential energy from the inductive and Josephson elements.

Classical one-fluxon states correspond to minima of the potential energy $\mathcal{V}^-$ with respect to flux variables φ_i^-, as shown in Fig. 3(a) for $N = 3$, describing a single fluxon trapped inside the superinductor ring surrounding the lattice in Fig. 2(b). We are considering henceforth the situation in
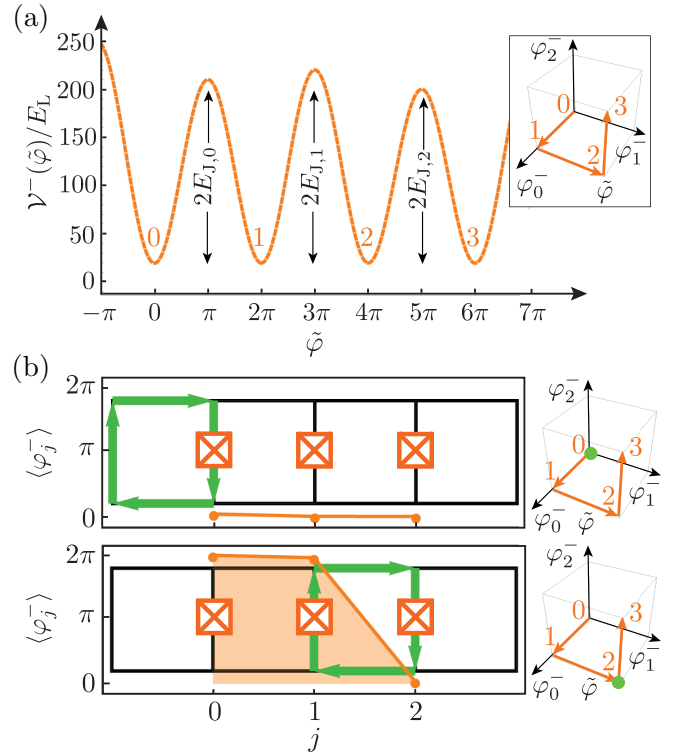

FIG. 3. Effective one-dimensional fluxon potential. (a) The classical potential for one-fluxon dynamics has four degenerate minima separated by Josephson energy barriers. The insets show that in $(\varphi_0^-, \varphi_1^-, \varphi_2^-)$ space the variable $\tilde{\varphi}$ traverses the edges of a hypercube between the four minima [see Eq. (7)]. (b) The one-fluxon state consists of a kink in the superconducting phase. If the kink occurs between junctions j and $j + 1$, in the limit $E_J \gg E_L$, the dominant current circulation (green arrows) occurs on the loop delimited by the two junctions. The circulating currents on the neighboring loops are suppressed by a factor of $\sim E_J/E_L$.

which one flux quantum is threaded through the superinductor ring by choosing $\varphi_{\text{ext},0} = 2\pi$, $\varphi_{\text{ext},i} = 0$ for $1 \leqslant i \leqslant N$. This guarantees that one-fluxon states are global minima of $\mathcal{V}^-$ (see Appendix A). These states are the $N + 1$ configurations of the superconducting phase ($k = 0, \ldots, N$),

$$(\varphi_i^-)^{(k)} \approx 2\pi, \quad 0 \leqslant i < k,$$
$$\approx 0, \quad k \leqslant i \leqslant N, \tag{7}$$

corresponding to kinks in the expectation value of the field φ_i^- as a function of i, as shown in Fig. 3(b).

The expressions in Eq. (7) are not exact minima of the potential energy $\mathcal{V}^-$ due to the quadratic contributions of the inductive energy terms $\propto E_L$. These deviations give rise to single vortices of persistent current localized at the position of the kink. The green arrows in Fig. 3(b) show the expectation values of currents $\frac{\Phi_0}{2\pi}I_{J,i} = E_{J,i}\sin(\varphi_i^-)$, $\frac{\Phi_0}{2\pi}I_i^- = \sqrt{2}E_L(\varphi_{i+1}^- - \varphi_i^- - \varphi_{\text{ext},i+1})$. The confinement of the persistent currents is essential to enable the local control of the potential energy, and it follows from the choice of energy scales $E_L \ll E_J$ in Eq. (6).

In the one-fluxon manifold, the relevant variable is the position of the kink. To parametrize this position, we define

the variable $\tilde{\varphi}$ along the curve in the $(\varphi_0^-, \varphi_1^-, \ldots, \varphi_{N-1}^-)$ space which contains the minima of the potential energy and their connections along classical instanton trajectories [52,53]. For example, for $N = 3$, the potential $\mathcal{V}^-(\tilde{\varphi})$ plotted in Fig. 3(a) has degenerate minima at points labeled $0, \ldots, 3$, corresponding to four classical one-fluxon states along the curve $\tilde{\varphi}$ represented in the inset. The minima are labeled by the position of the kink, where 0 stands for no kink, 1 stands for the kink at the first junction, etc. [Fig. 3(b)].

III. TIGHT-BINDING DESCRIPTION

The charging energy $\mathcal{T}^-$ gives rise to quantum tunneling between one-fluxon states. Projecting $\mathcal{H}^-$ into the one-fluxon manifold yields a quantum tight-binding model

$$h^- = \sum_{i=0}^{N-1} \epsilon_i |i\rangle\langle i| - \sum_{i=0}^{N-2} t_i |i\rangle\langle i+1| + \text{H.c.}, \quad (8)$$

where $|i\rangle$ denotes the one-fluxon state at $i = 0, \ldots, N-1$. We have retained in h^- only the next-neighbor contributions [see Fig. 2(c)], as tunnel rates drop exponentially with distance. The on-site energies are $\epsilon_i \approx \frac{1}{2}\hbar\omega_i$, where $\omega_i = \sqrt{8 E_{\mathrm{C},i}^- E_{\mathrm{J},i}}$ is the Josephson plasma frequency. The tunneling rate [52–55] (the splitting of the N-fold degenerate low-lying manifold of classical minima) is exponentially small $t_i \propto e^{-\sqrt{8 E_{\mathrm{J},i}/E_{\mathrm{C},i}^-}}$ and becomes zero in the classical limit $E_{\mathrm{J},i} \gg E_{\mathrm{C},i}^-$. Since the precise value of the numerical prefactor depends on the shape of the potential, in the following we solve for the tunnel rates exactly via numerical diagonalization.

The low-energy one-fluxon manifold is separated from the remainder of the spectrum either by a gap of order $(2\pi)^2 E_{\mathrm{L}}$, corresponding to the creation of an additional fluxon or antifluxon in Eq. (6), which amounts to a repulsive interaction, or by an energy scale corresponding to the Josephson plasma frequency, which amounts to an on-site excitation into a higher-energy eigenstate of the local potential well. If multiple fluxons are inserted into the array, it is expected that the vortex dynamics closely resembles that of a gas of hardcore bosons with an exponentially suppressed long-range repulsive interaction whose distance scale is the size of a single fluxon and is roughly proportional to $(E_{\mathrm{L}}/E_{\mathrm{J}})^{1/2}$ [50]. This statement holds for energy scales comparable to the bandwidth t_i and far inferior to the gap. In particular, the Mott insulating state of one fluxon per loop corresponds to the band insulator obtained by occupying all states of the (band) spectrum of Eq. (8) with $\epsilon_i = \epsilon$ and $t_i = t$. Note that fluxon dynamics is dual to that of bosons on a two-leg Josephson ladder, which have a rich ground-state phase diagram depending on external flux and boson density [50,56–59].

We validate our semiclassical arguments with an exact numerical diagonalization. For this purpose, we consider $N = 3$ junctions,

$$\mathcal{H}^- = 4 E_{\mathrm{C}}^- [(n_0^-)^2 + (n_1^-)^2 + (n_2^-)^2] + \mathcal{V}^-(\varphi_0^-, \varphi_1^-, \varphi_2^-). \quad (9)$$

To numerically diagonalize $\mathcal{H}^-$ we consider the equivalent eigenvalue problem and solve it by a finite-difference method [60] complemented by exact diagonalization (the procedure
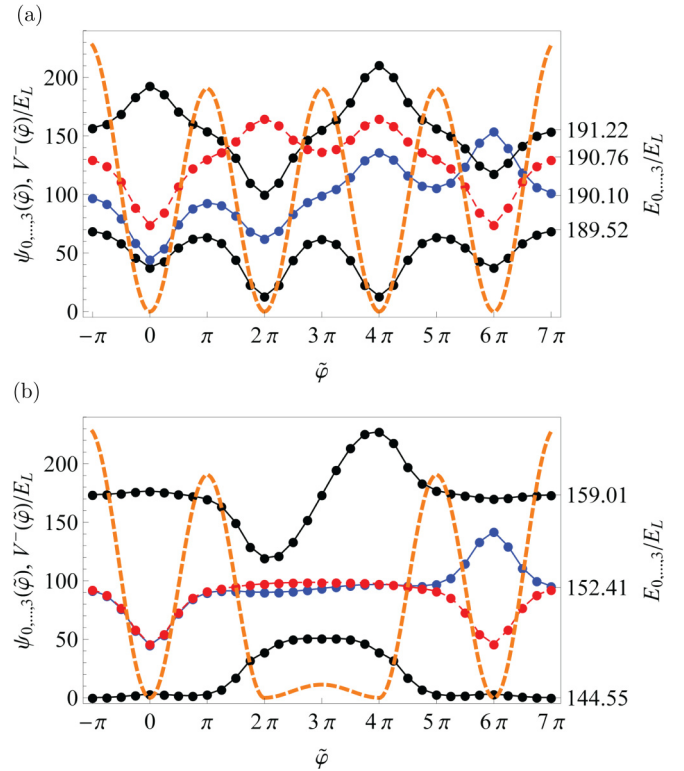

FIG. 4. Low-lying spectrum and wave functions for the lowest four states (represented in ascending order with respect to their energy by solid black, dashed red, solid blue, and solid black curves) for a three-junction circuit with $E_{\mathrm{C}} = 10$ and $E_{\mathrm{J}0} = E_{\mathrm{J}2} = 100 = \eta E_{\mathrm{J}1}$ in units of $E_{\mathrm{L}} = \frac{(\Phi_0/2\pi)^2}{2L}$, with (a) $\eta = 1$ and (b) $\eta = 10$. We show with orange dashed lines the potential energy $\mathcal{V}^-(\tilde{\varphi})$ (left vertical axis). The wave functions (in arbitrary units) are offset by their eigenenergies (right vertical axis). For (b), the first and second excited states are intragap boundary-localized excitations of the one-fluxon tight-binding model. The points represent the values obtained from numerical diagonalization, and the lines are direct connections.

is detailed in Appendix C). We plot the wave function $\psi(\varphi_0^-, \varphi_1^-, \varphi_2^-)$, along the $\tilde{\varphi}$ coordinate, and the eigenvalues of lowest-lying states in Fig. 4(a). Due to the action of the charging (Laplacian) terms, there is some leakage of the wave functions along the coordinates perpendicular to the curve parametrized by $\tilde{\varphi}$. This effect is taken into account in the multidimensional numerical diagonalization.

Tunneling amplitudes can be tuned to yield a topological band structure in one dimension. Here, we discuss a fluxon analog of the Su-Schrieffer-Heeger model [61,62], originally proposed to describe the electronic structure of polyacetylene, which sustains a symmetry-protected topological phase with fractionally charged edge states [63–65]. This is achieved in the one-fluxon model (8) by dimerizing the Josephson energy $E_{\mathrm{J},j} = E_{\mathrm{J}} + (-1)^{j+1}\delta$, with $E_{\mathrm{J}} > \delta > 0$ and $j = 0, \ldots, N-1$. A pair of exponentially boundary localized states is observable for odd $N \geqslant 3$. In Fig. 4(b) we show the low-lying energies and eigenstates for the minimal length of $N = 3$ junctions with $E_{\mathrm{J},0} = E_{\mathrm{J},2} = 10 E_{\mathrm{J},1}$ and $E_{\mathrm{C}}^- = E_{\mathrm{J},0}/10$. The effect of enhanced tunneling on the

middle junction is to split the states corresponding to fluxons localized on the two central loops, leading to a large energy gap. The remaining two intragap states correspond to fluxons localized on the end loops. Their hybridization must vanish exponentially for increasing N. As long as the dimerization relation is preserved (i.e., the disorder does not close the band gap), disorder in the tunneling rates of the effective tight-binding model (8) does not induce a significant splitting of the two bound states. On the other hand, the degeneracy is vulnerable to flux noise, which amounts to on-site disorder in Eq. (8) (see Appendix D for a discussion of the effect of disorders).

The levels of the dimerized low-energy model can be filled as fluxons are added to the system. When one inserts $m = \frac{N+1}{2} + 1$ fluxons, the ground state has two intragap boundary-localized excitations [62,65–67], which could be used for the implementation of a superconducting qubit. This may offer an alternative to fault-tolerant quantum computation via topological protection, similar to the 0-π qubit [60,68–73].

IV. CONCLUSION

We have presented an alternative path to perform quantum simulation, moving away from the well-known microwave photon architectures to a concept based on fluxon dynamics in networks of Josephson junctions. Unlike photons, fluxons can be individually trapped inside superinductor loops, and their number m can be stable for durations practically infinite compared to the experimental timescales. The control and readout of the states could be performed using the standard tools of cQED. Dispersive quantum nondemolition measurements [74] could be adapted to access the local density of states in such circuits by using locally coupled rf antennas.

We have discussed the possible experimental limitations of this platform and argued that the current quantum fluxon model is robust for networks containing up to ~50 lattice sites, after which the transmission-line modes of the circuit can interfere with the fluxon modes. This limit could be increased by using more sophisticated circuit fabrication technologies, which can remove most of the backplane dielectric via etching and thus decrease the self-capacitance [75].

The power of quantum fluxonics is illustrated by the implementation of the Su-Schrieffer-Heeger model in the one-fluxon subspace. Probes of the Zak geometric phase [76] classifying the topological state of a long circuit could be devised, as exemplified for microwave photons in a dimerized one-dimensional quantum LC array [77]. The purpose of this proposal is not to introduce a quantum simulator for a specific model, but rather an entirely different platform. Finally, we note that, beyond the scope of quantum simulation, fluxons could be appealing for on-chip quantum state transfer [78,79] and routing [80].

ACKNOWLEDGMENTS

APPENDIX A: FLUXON INSERTION

In this Appendix, we provide a more detailed discussion of the protocol for fluxon insertion. We consider the circuit in Fig. 5, in which L is a superinductance [35], as described in the main text, and the loop is closed by an input Josephson junction with Josephson energy $E_{\text{J,in}}$ approximately 100 times the charging energy $E_{\text{C,in}}$. Before we review the time-dependent protocol introduced in the main text, we derive the equations of motion and the potential energy for the circuit of Fig. 5. The physics of the input junction is analogous to that of a weak link interrupting a loop of a superconductor [81–83].

We now write a system of classical equations of motion for branch fluxes and currents corresponding to the Josephson junction and the inductor. These can be represented in terms of node variables $\Phi_{\text{J}} = \phi_1 - \phi_g$ and $\Phi_{\text{L}} = \phi_1 - \phi_g + \Phi_{\text{ext}}$, respectively, from which we derive the loop equation for branch fluxes:

$$\Phi_{\text{L}} = \Phi_{\text{J}} + \Phi_{\text{ext}}. \qquad (A1)$$

Current conservation at node 1 means

$$I_{\text{J}} + I_{\text{L}} = C_{\text{J}} \ddot{\phi}_1. \qquad (A2)$$

Equations (A1) and (A2) underlie the derivation of the Hamiltonian of the circuit in Fig. 5(a) based on the rules of circuit quantization [84,85].
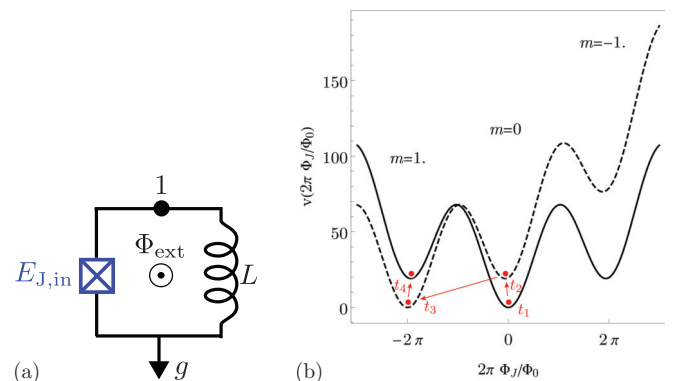

FIG. 5. (a) Circuit layout illustrating the conventions in the text. (b) Reduced potential function $v(\varphi_J)$ for the circuit in (a) at $\varphi_{\text{ext}} = 0$ (black solid line) and $\varphi_{\text{ext}} = 2\pi$ (black dashed line). The times t_1, t_2, t_3, t_4 correspond to those represented in Fig. 1 of the main text, and the red arrows and circles indicate the four stages of the insertion of one fluxon. The integers m above the three central minima indicate the value of the fluxoid, $2\pi m$, from Eq. (A9) or its equivalent (A10).

The purpose of this section is to derive the potential energy and its stationarity conditions. To this end, let us set the right member of Eq. (A2) to zero and denote the loop current with the symbol I, with the following sign convention:

$$I = I_{\mathrm{J}} = -I_{\mathrm{L}}. \tag{A3}$$

The current around the loop can be related to the phase difference across the Josephson junction in the following way. Let

$$\varphi_{\mathrm{J}} \equiv 2\pi \frac{\Phi_{\mathrm{J}}}{\Phi_0} \bmod 2\pi \tag{A4}$$

be the superconducting phase difference across the Josephson junction. It is useful to explicitly introduce an integer m such that the equality modulo multiples of 2π becomes

$$\varphi_{\mathrm{J}} = 2\pi \frac{\Phi_{\mathrm{J}}}{\Phi_0} + 2\pi m. \tag{A5}$$

The phase variable φ_{J} is defined to be compact on the interval $(-\pi, \pi]$. It is related to the current through the Josephson junction through the Josephson relation

$$I = I_{\mathrm{c}} \sin(\varphi_{\mathrm{J}}), \varphi_{\mathrm{J}} = \sin^{-1}\left(\frac{I}{I_{\mathrm{c}}}\right), \tag{A6}$$

where I_{c} is the critical current. It is related to the Josephson energy through the relation $E_{\mathrm{J,in}} = I_{\mathrm{c}}\Phi_0/(2\pi)$.

The current I is also related to the flux through the inductor Φ_{L} through the constitutive equation

$$\Phi_{\mathrm{L}} = -LI, \tag{A7}$$

where we have used Eq. (A3).

We can now use the Josephson relation (A6), the equation relating the flux and phase variables (A5), and the constitutive equation of the inductor (A7) together with the loop equation (A1) to obtain

$$-LI = \frac{\varphi_{\mathrm{J}}}{2\pi}\Phi_0 - m\Phi_0 + \Phi_{\mathrm{ext}}. \tag{A8}$$

Rearranging terms, this gives

$$\frac{\varphi_{\mathrm{J}}}{2\pi}\Phi_0 + (LI + \Phi_{\mathrm{ext}}) = m\Phi_0. \tag{A9}$$

The quantity on the right-hand side is the London fluxoid. The term in the parentheses is the total flux through the superconducting loop, composed of the kinetic flux LI from the loop inductance L and the external flux Φ_{ext}. This is the fluxoid quantization condition [83,86].

Using the Josephson relation (A6) in Eq. (A9), we arrive at the transcendental equation

$$\varphi_{\mathrm{J}} - 2\pi m + 2\pi \frac{\Phi_{\mathrm{ext}}}{\Phi_0} = -\sin(\varphi_{\mathrm{J}}). \tag{A10}$$

Recall that φ_{J} is defined on the compact interval $(-\pi, \pi]$. Different solutions of the transcendental equation above are obtained by varying m at fixed Φ_{ext}. Alternatively, one may use the relation between Φ_{J} and φ_{J}, Eq. (A5), and solve a transcendental equation for the real variable, the flux:

$$2\pi\Phi_{\mathrm{J}}/\Phi_0 + 2\pi\Phi_{\mathrm{ext}}/\Phi_0 = -\sin(2\pi\Phi_{\mathrm{J}}/\Phi_0). \tag{A11}$$

Equations (A10) and (A11) are equivalent, and they serve to distinguish between the compact phase variable φ_{J} and the real

flux variable Φ_{J}. The equation for the compact phase variable φ_{J} necessarily contains the London fluxoid $2\pi m$ [in units of $\Phi_0/(2\pi)$].

Equation (A11) is a stationarity condition for the dimensionless potential energy [consistent with the equations of motion (A1) and (A2)]

$$v\left(2\pi\frac{\Phi_{\mathrm{J}}}{\Phi_0}\right) = \left[1 - \cos\left(2\pi\frac{\Phi_{\mathrm{J}}}{\Phi_0}\right)\right] + 2\pi\frac{(\Phi_{\mathrm{J}} + \Phi_{\mathrm{ext}})^2}{2\Phi_{\mathrm{c}}\Phi_0}, \tag{A12}$$

where we have introduced the critical kinetic flux $\Phi_{\mathrm{c}} = LI_{\mathrm{c}}$. This function is plotted in Fig. 5(b) for two values of the external flux $\Phi_{\mathrm{ext}} = 0$ (solid line) and Φ_0 (dashed line). The minima of the potential energy are labeled by their respective values of the fluxoid $2\pi m$, as obtained from the solution to the transcendental equation (A10).

The fluxon insertion protocol relies on that of Masluk *et al.* [35]. The input junction is addressable by means of the antenna connected across a shunt capacitance C_{S}. The superinductor loop is threaded by external flux Φ_{ext}. The insertion of one fluxon entails increasing the fluxoid from $m = 0$ to $m = 1$ in units of the superconducting flux quantum in the following sequence: Before t_1 at zero external flux, the system is in its classical ground state corresponding to $m = 0$. At t_1, the flux is increased to Φ_0, maintaining the system in the metastable minimum. Between t_2 and t_3 a high-amplitude drive is applied to lower the effective Josephson potential $E_{\mathrm{J,in}}$, which prompts a spontaneous relaxation of the system to the lower-energy state at $m = 1$. At t_4, the flux is turned back to zero, thereby placing the system in an (excited) metastable state at $m = 1$. The procedure can be iterated to insert additional fluxons. To insert m fluxons, a field $\Phi_{\mathrm{ext}} = m\Phi_0$ would be necessary in order to turn the m-fluxon minimum into a global minimum at time t_2.

APPENDIX B: DERIVATION OF THE CIRCUIT HAMILTONIAN FOR THE JOSEPHSON TRANSMISSION LINE

Consider the circuit in Fig. 6. We follow Refs. [84,85] to quantize the circuit. We will generalize our results to $2N$ superconducting islands but keep the calculation concrete at $N = 3$ for brevity. Below, g denotes the ground node, to
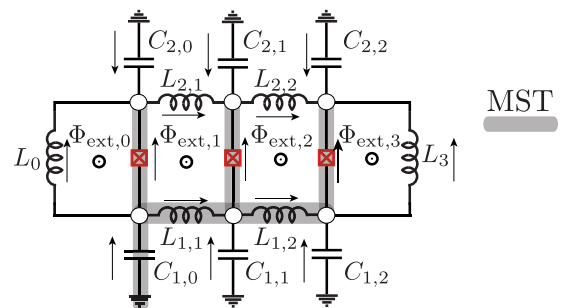

FIG. 6. $N = 3$ junction circuit with open boundaries. The minimum spanning tree (MST) [84] is highlighted in gray. The junctions, not labeled above, are characterized by Josephson energy $E_{\mathrm{J},j}$ and capacitance $C_{\mathrm{J},j}$, $j = 0, 1, 2$.

which superconducting island α, j, with $\alpha = 1, 2$ and $j = 0, 1, 2$, is connected via capacitance $C_{\alpha,j}$. The Josephson energy of the jth junction is $E_{J,j} = \frac{\hbar I_{c,j}}{2e}$, where $I_{c,j}$ denotes the critical current on the jth junction. The capacitance of each junction is $C_{J,j}$. The minimum spanning tree (MST) covering the six active nodes αj for $\alpha = 1, 2$, $j = 0, 1, 2$ is highlighted in gray in Fig. 6. The loop equations in terms of branch variables (labeled according to Fig. 6) are

$$\Phi_{C_{1,1}} - \Phi_{L_{1,1}} - \Phi_{C_{1,0}} = 0,$$
$$\Phi_{C_{1,2}} - \Phi_{L_{1,2}} - \Phi_{L_{1,1}} - \Phi_{C_{1,0}} = 0,$$
$$\Phi_{C_{2,0}} - \Phi_{E_{J,0}} - \Phi_{C_{1,0}} = 0,$$
$$\Phi_{C_{2,1}} - \Phi_{E_{J,1}} - \Phi_{L_{1,1}} - \Phi_{C_{1,0}} = 0,$$
$$\Phi_{C_{2,2}} - \Phi_{E_{J,2}} - \Phi_{L_{1,2}} - \Phi_{L_{1,1}} - \Phi_{C_{1,0}} = 0, \quad \text{(B1)}$$
$$\Phi_{E_{J,0}} - \Phi_{L_0} = \Phi_{\text{ext},0},$$
$$\Phi_{E_{J,1}} - \Phi_{L_{2,1}} - \Phi_{E_{J,0}} + \Phi_{L_{1,1}} = \Phi_{\text{ext},1},$$
$$\Phi_{E_{J,2}} - \Phi_{L_{2,2}} - \Phi_{E_{J,1}} + \Phi_{L_{1,2}} = \Phi_{\text{ext},2},$$
$$-\Phi_{E_{J,2}} + \Phi_{L_3} = \Phi_{\text{ext},3}.$$

The branch fluxes for branches that belong to the MST can be reexpressed in terms of node fluxes,

$$\Phi_{E_{J,0}} = \phi_{2,0} - \phi_{1,0}, \qquad \Phi_{E_{J,1}} = \phi_{2,1} - \phi_{1,1},$$
$$\Phi_{E_{J,2}} = \phi_{2,2} - \phi_{1,2}, \qquad \Phi_{L_{1,1}} = \phi_{1,1} - \phi_{1,0}, \quad \text{(B2)}$$
$$\Phi_{L_{1,2}} = \phi_{1,2} - \phi_{1,1}, \qquad \Phi_{C_{1,0}} = \phi_{1,0} - \phi_g.$$

Placing these in the loop equations (B1), we obtain

$$\Phi_{C_{1,1}} = \phi_{1,1} - \phi_g, \quad \Phi_{C_{1,2}} = \phi_{1,2} - \phi_g,$$
$$\Phi_{C_{2,0}} = \phi_{2,0} - \phi_g, \quad \Phi_{C_{2,1}} = \phi_{2,1} - \phi_g,$$
$$\Phi_{C_{2,2}} = \phi_{2,2} - \phi_g,$$
$$\Phi_{L_0} = \phi_{2,0} - \phi_{1,0} - \Phi_{\text{ext},0}, \quad \Phi_{L_3} = \phi_{2,2} - \phi_{1,2} + \Phi_{\text{ext},3},$$
$$\Phi_{L_{2,1}} = \phi_{2,1} - \phi_{2,0} - \Phi_{\text{ext},1}, \quad \Phi_{L_{2,2}} = \phi_{2,2} - \phi_{2,1} - \Phi_{\text{ext},2}.$$
$$\text{(B3)}$$

Substituting (B2) and (B3) into the Kirchoff node equations, we find equations of motion α, i:

$$1,0 : \ -\frac{\phi_{2,0} - \phi_{1,0} - \Phi_{\text{ext},0}}{L_0} - I_{c,0}\sin\left(2\pi\frac{\phi_{2,0} - \phi_{1,0}}{\phi_0}\right) + \frac{\phi_{1,1} - \phi_{1,0}}{L_{1,1}} = C_{1,0}(\ddot{\phi}_{1,0} - \ddot{\phi}_g) - C_0(\ddot{\phi}_{2,0} - \ddot{\phi}_{1,0}),$$

$$2,0 : \ +\frac{\phi_{2,0} - \phi_{1,0} - \Phi_{\text{ext},0}}{L_0} + I_{c,0}\sin\left(2\pi\frac{\phi_{2,0} - \phi_{1,0}}{\phi_0}\right) - \frac{\phi_{2,1} - \phi_{2,0} - \Phi_{\text{ext},1}}{L_{2,1}} = C_{2,0}(\ddot{\phi}_{2,0} - \ddot{\phi}_g) + C_0(\ddot{\phi}_{2,0} - \ddot{\phi}_{1,0}),$$

$$1,1 : \ \frac{\phi_{1,1} - \phi_{1,0}}{L_{1,1}} - I_{c,1}\sin\left(2\pi\frac{\phi_{2,1} - \phi_{1,1}}{\phi_0}\right) - \frac{\phi_{1,2} - \phi_{1,1}}{L_{1,2}} = C_{1,1}(\ddot{\phi}_{1,1} - \ddot{\phi}_g) - C_1(\ddot{\phi}_{2,1} - \ddot{\phi}_{1,1}), \quad \text{(B4)}$$

$$2,1 : \ \frac{\phi_{2,1} - \phi_{2,0} - \Phi_{\text{ext1}}}{L_{2,1}} + I_{c,1}\sin\left(2\pi\frac{\phi_{2,1} - \phi_{1,1}}{\phi_0}\right) - \frac{\phi_{2,2} - \phi_{2,1} - \Phi_{\text{ext2}}}{L_{2,2}} = C_{2,1}(\ddot{\phi}_{2,1} - \ddot{\phi}_g) + C_1(\ddot{\phi}_{2,1} - \ddot{\phi}_{1,1}),$$

$$1,2 : \ +\frac{\phi_{1,2} - \phi_{1,1}}{L_{1,2}} - I_{c,2}\sin\left(2\pi\frac{\phi_{2,2} - \phi_{1,2}}{\phi_0}\right) - \frac{\phi_{2,2} - \phi_{1,2} + \Phi_{\text{ext3}}}{L_3} = C_{1,2}(\ddot{\phi}_{1,2} - \ddot{\phi}_g) - C_2(\ddot{\phi}_{2,2} - \ddot{\phi}_{1,2}),$$

$$2,2 : \ +\frac{\phi_{2,2} - \phi_{2,1} - \Phi_{\text{ext},2}}{L_{2,2}} + I_{c,2}\sin\left(2\pi\frac{\phi_{2,2} - \phi_{1,2}}{\phi_0}\right) + \frac{\phi_{2,2} - \phi_{1,2} + \Phi_{\text{ext3}}}{L_3} = C_{2,2}(\ddot{\phi}_{2,2} - \ddot{\phi}_g) + C_2(\ddot{\phi}_{2,2} - \ddot{\phi}_{1,2}).$$

These are Euler-Lagrange equations for the following Lagrangian (expressed now in terms of N; to retrieve the previous equations, one would set $N = 3$):

$$\mathcal{L} = \sum_{j=0}^{N-1}\frac{1}{2}C_j(\dot{\phi}_{2,j} - \dot{\phi}_{1,j})^2 + \sum_{j=0}^{N-1}\sum_{\alpha=1,2}\frac{1}{2}C_{\alpha,i}(\dot{\phi}_{\alpha,i} - \dot{\phi}_g)^2 - \sum_{j=0}^{N-2}\left[\frac{(\phi_{1,j+1} - \phi_{1,j})^2}{2L_{1,j+1}} + \frac{(\phi_{2,j+1} - \phi_{2,j} - \Phi_{\text{ext},j+1})^2}{2L_{2,j+1}}\right]$$

$$- \frac{(\phi_{2,0} - \phi_{1,0} - \Phi_{\text{ext},0})^2}{2L_0} - \frac{(\phi_{2,N-1} - \phi_{1,N-1} + \Phi_{\text{ext},N})^2}{2L_N} + \sum_{j=0}^{N-1}E_{J,j}\left[1 - \cos\left(2\pi\frac{\phi_{2,j} - \phi_{1,j}}{\phi_0}\right)\right]. \quad \text{(B5)}$$

Now set the longitudinal inductances to all be equal, $L_{\alpha,i} = L$, and the terminal inductors to a value that ensures that all loop inductances are constant across the circuit $L_0 = L_N = 2L$. Further, let the capacitance to ground of each superconducting island be $C_{\alpha,i} = C_0$ for $i = 0, \ldots, N-1$ and $\alpha = 1, 2$. These assignments agree with the particular choices denoted in Fig. 2(b) in the main text. We now introduce new coordinates,

$$\phi_j^{\pm} = \phi_{2,j} \pm \phi_{1,j}. \quad \text{(B6)}$$

In terms of these fields the charging energy is rearranged into

$$\frac{1}{2}C_0(\dot{\phi}_{j,0} - \dot{\phi}_g)^2 + \frac{1}{2}C_0(\dot{\phi}_{j,1} - \dot{\phi}_g)^2 \equiv \frac{1}{2}C_0(A^2 + B^2) = \frac{1}{2}C_0\frac{(A+B)^2 + (A-B)^2}{2} = C_0[(\dot{\phi}_{j^+}/2 - \dot{\phi}_g)^2 + (\dot{\phi}_{j^-}/2)^2],$$
$$\text{(B7)}$$

and the longitudinal inductive elements give rise to

$$\frac{(\phi_{1,j+1} - \phi_{1,j})^2}{2L} + \frac{(\phi_{2,j+1} - \phi_{2,j} - \Phi_{\text{ext},j+1})^2}{2L} = \frac{1}{4L}[(\phi_{j+1}^+ - \phi_j^+ - \Phi_{\text{ext},j+1})^2 + (\phi_{j+1}^- - \phi_j^- - \Phi_{\text{ext},j+1})^2]. \quad \text{(B8)}$$

Additionally, the inductive terms for the two end loops transform to

$$\frac{(\phi_{2,0} - \phi_{1,0} - \Phi_{\text{ext},0})^2}{2 \times 2L} = \frac{(\phi_0^- - \Phi_{\text{ext},0})^2}{2 \times 2L}, \quad \frac{(\phi_{2,N-1} - \phi_{1,N-1} + \Phi_{\text{ext},N})^2}{2 \times 2L} = \frac{(\phi_{N-1}^- + \Phi_{\text{ext},N})^2}{2 \times 2L}. \quad \text{(B9)}$$

In terms of the new coordinates introduced in (B6) the Lagrangian of Eq. (B5) becomes

$$\mathcal{L} = \sum_{j=0}^{N-1} \frac{C_{J,j}}{2}(\dot{\phi}_{j-})^2 + \sum_{j=0}^{N-1} \frac{C_0}{4}[(\dot{\phi}_{j+} - 2\dot{\phi}_g)^2 + (\dot{\phi}_{j-})^2] - \sum_{j=0}^{N-2} \frac{1}{4L}[(\phi_{j+1}^+ - \phi_j^+ - \Phi_{\text{ext},j+1})^2 + (\phi_{j+1}^- - \phi_j^- - \Phi_{\text{ext},j+1})^2]$$

$$- \frac{1}{4L}[(\phi_0^- - \Phi_{\text{ext},0})^2 + (\phi_{N-1}^- + \Phi_{\text{ext},N})^2] + \sum_{j=0}^{N-1} E_{J,j}\left[1 - \cos\left(2\pi \frac{\phi_j^-}{\Phi_0}\right)\right]. \quad \text{(B10)}$$

The canonically conjugate momenta corresponding to the variables introduced in Eq. (B6) are

$$\frac{\partial \mathcal{L}}{\partial \dot{\phi}_{j-}} \equiv Q_j^- = (C_{J,j} + C_0/2)\dot{\phi}_{j-}, \quad \frac{\partial \mathcal{L}}{\partial \dot{\phi}_{j+}} \equiv Q_j^+ = (C_0/2)(\dot{\phi}_{j+} - 2\dot{\phi}_g),$$

$$\frac{\partial \mathcal{L}}{\partial \dot{\phi}_g} \equiv Q_g = -\sum_{j=0}^{N-1} C_0(\dot{\phi}_{j+} - 2\dot{\phi}_g). \quad \text{(B11)}$$

After a Legendre transform, $\mathcal{H} \equiv Q_g \dot{\phi}_g + \sum_{j=0}^{N-1} \sum_{\alpha=\pm} Q_j^\alpha \dot{\phi}_{j\alpha} - \mathcal{L}$, and promoting classical degrees of freedom to quantum operators, we find

$$\mathcal{H} = \sum_{j=0}^{N-1} \frac{(Q_j^+)^2}{2(C_0/2)} + \sum_{j=0}^{N-1} \frac{(Q_j^-)^2}{2(C_{J,j} + C_0/2)} + \sum_{j=0}^{N-2} \frac{1}{4L}[(\phi_{j+1}^+ - \phi_j^+ - \Phi_{\text{ext},j+1})^2 + (\phi_{j+1}^- - \phi_j^- - \Phi_{\text{ext},j+1})^2]$$

$$+ \frac{1}{4L}[(\phi_0^- - \Phi_{\text{ext},0})^2 + (\phi_{N-1}^- + \Phi_{\text{ext},N})^2] - \sum_{j=0}^{N-1} E_{J,j}\left[1 - \cos\left(2\pi \frac{\phi_j^-}{\phi_0}\right)\right]. \quad \text{(B12)}$$

We introduce, as in the main text, a dimensionless variable for the flux $\varphi_j^\alpha = 2\pi \phi_j^\alpha / \Phi_0$ and the canonically conjugate Cooper pair number $n_j^\alpha = \frac{Q_j^\alpha}{2e}$ for $j = 0, \ldots, N-1$ and $\alpha = \pm$. We also introduce energy scales associated with charging and inductive circuit elements,

$$E_C^+ = \frac{e^2}{2(C_0/2)}, \quad E_L = \frac{[\Phi_0/(2\pi)]^2}{2L}, \quad E_{C,j}^- = \frac{e^2}{2(C_{J,j} + C_0/2)}, \quad \text{(B13)}$$

as well as dimensionless flux variables

$$\varphi_{\text{ext},j} = \frac{2\pi}{\Phi_0}\Phi_{\text{ext},j}. \quad \text{(B14)}$$

The Hamiltonian reads

$$\mathcal{H} = \mathcal{H}^+ + \mathcal{H}^-, \quad \text{(B15)}$$

where

$$\mathcal{H} = \sum_{j=0}^{N-1} 4E_C^+ (n_j^+)^2 + \sum_{j=0}^{N-1} 4E_{C,j}^- (n_j^-)^2 + \sum_{j=0}^{N-2} \frac{E_L}{2}[(\varphi_{j+1}^+ - \varphi_j^+ - \varphi_{\text{ext},j+1})^2 + (\varphi_{j+1}^- - \varphi_j^- - \varphi_{\text{ext},j+1})^2]$$

$$+ \frac{E_L}{2}[(\varphi_0^- - \varphi_{\text{ext},0})^2 + (\varphi_{N-1}^- + \varphi_{\text{ext},N})^2] - \sum_{j=0}^{N-1} E_{J,j}[1 - \cos(\varphi_j^-)]. \quad \text{(B16)}$$
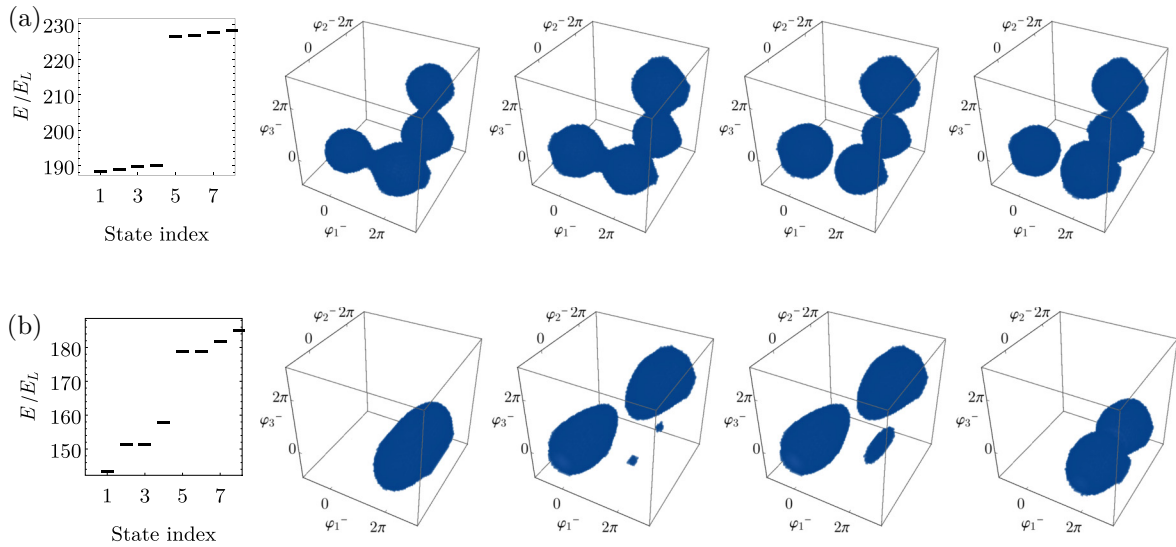
This is the Hamiltonian used in the main text.

FIG. 7. Three-dimensional density plots (opaque volumes signify that the absolute value of the probability density exceeds 10^{-3}) for the first four eigenstates of $\mathcal{H}^-$ in Eq. (9) obtained from the finite-differences solution with $N_p = 17$. The low-lying energies are represented in the leftmost panels. We set $E_C = E_{J,0} \times 10^{-1}$, $E_{J,0} = \eta \times E_{J,1} = E_{J,2}$ in units of $E_L = \frac{(\Phi_0/2\pi)^2}{2L}$, with (a) $\eta = 1$ and (b) $\eta = 10$, corresponding to the values chosen in Fig. 4 of the main text. In (a), the eigenvalues of the first five states, in units of E_L, are 189.51, 190.10, 190.75, 191.22, and 227.49, respectively. In (b), the first five eigenvalues are 144.55, 152.34, 152.41, 159.01, and 179.91, respectively.

APPENDIX C: NUMERICAL METHODS

In this Appendix we detail the solution to Eq. (9) of the main text. For three junctions, the quantum Hamiltonian in the antisymmetric sector reads

$$\mathcal{H}^- \approx 4E_C[(n_0^-)^2 + (n_1^-)^2 + (n_2^-)^2] + \mathcal{V}^-(\varphi_0^-, \varphi_1^-, \varphi_2^-),$$
(C1)

where one flux quantum is threaded through the entire circuit. The latter condition makes the classical global minimum correspond to fluxoid $m = 1$ [in analogy with the point marked t_3 in Fig. 5(b)]. We choose a gauge such that $\varphi_{\text{ext},0} = 2\pi$ and $\varphi_{\text{ext},i} = 0$ for $i = 1, 2, 3$. Moreover, making the inductances of the four elementary loops in the circuit equal ensures that the global minimum of the potential energy is fourfold degenerate: this is the underlying tight-binding lattice.

Writing $n_i^- = -i\frac{\partial}{\partial\varphi_i^-}$, the associated Schrödinger equation takes the form of a differential eigenvalue equation,

$$\mathcal{H}^-\left(\left\{-i\frac{\partial}{\partial\varphi_i^-}, \varphi_i^- \,\middle|\, i = 0, \ldots, 2\right\}\right)\psi = E\psi.$$
(C2)

This eigenvalue equation can be solved by finite-difference methods [60]. With one flux quantum threaded through the loop, as explained in the previous paragraph, the lowest-energy manifold will contain only one-fluxon states, and therefore, we consider only the interval $(\varphi_0^-, \varphi_1^-, \varphi_2^-) \in [-\pi, 3\pi] \times [-\pi, 3\pi] \times [-\pi, 3\pi]$. This interval symmetrically contains the minima at 0 and 2π. We cover this interval by a uniform mesh of N_p points in each of the three directions. Local minima of the classical potential outside of the first octant are higher than the ones inside it by an energy approximately equal to $(2\pi)^2 E_L$, as follows from the expression of the potential energy in Eq. (B16), and their influence is neglected. We adapt the mesh size so that in the classical

limit, corresponding to vanishing charging energies $E_C = 0$, the lowest-energy eigenvalues and the corresponding wave functions agree with the minima of the classical potential. In Fig. 7 we show results for the uniform and dimerized lattices for a computation corresponding to $N = 3$ junctions and mesh size $N_p = 17$ along each axis. Diagonalization was performed with a Jacobi-Davidson routine in the MATHEMATICA package.

APPENDIX D: DISORDER EFFECTS

In the cQED implementation of the tight-binding model for fluxons, tunneling rate disorders would arise from the spread in the junction parameters $E_{J,i}$, $E_{C,i}^-$ in Eqs. (5) and (6) of the main text, whereas on-site disorders are induced by flux disorder at the level of the circuit, i.e., in the variables $\varphi_{\text{ext},i}$ in Eq. (6) of the main text. Based on this correspondence, we will show in this section that the degeneracy of the bound states in the circuit QED implementation of the Su-Schrieffer-Heeger model is fairly robust to junction imperfections. However, local flux noise will generally split the degenerate manifold.

In Fig. 8 we show typical values for the tunnel rate through a single junction as a function of the junction surface area, along with the expected spread caused by errors in the junction surface area of the order of 5% and 10%, respectively. We consider the following dependence for the tunnel rate on the Josephson and charging energies [55]:

$$t = 8\sqrt{\frac{E_J E_C}{\pi}}\left(\frac{E_J}{2E_C}\right)^{\frac{1}{4}} e^{-\sqrt{8E_J/E_C}}.$$
(D1)

Additionally, from the Ambegaokar-Baratoff [87] formula we may express

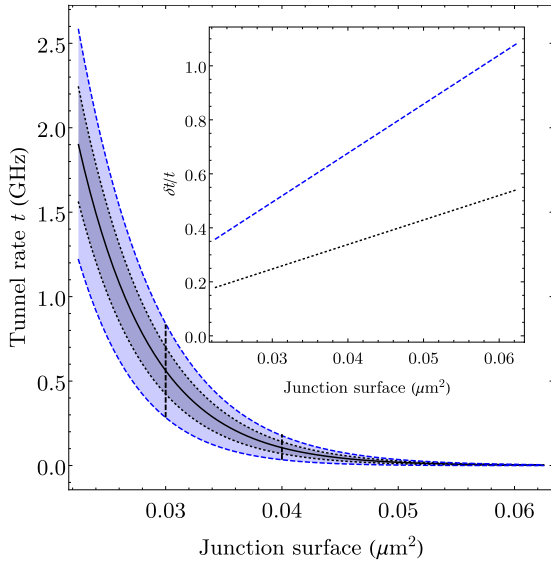$$E_J = h\frac{\Delta}{8e^2}\frac{1}{R_n(S)},$$
(D2)

FIG. 8. Typical tunnel rate for a Josephson junction as a function of junction surface area (solid black lines). The black dotted (blue dashed) lines together with the shaded region between them show the spread of the tunnel rate for a 5% (10%) error in the surface area. Thick black dashed lines serve as guides to the eye to illustrate a possible choice of two reference surface areas for the small and large junctions in the dimerized configuration. Inset: Fractional spread of the tunnel rate as a function of junction area for a 5% (black dotted line) and 10% (blue dashed line) tolerance in the junction surface area.

where h is Planck's constant, e is the electron charge, and $R_n(S)$ is the normal-state resistance. We take the typical dependence of the normal-state resistance on the surface area in the form $R_n(S) = \alpha_R/S$, where $\alpha = 100\,\Omega\,\mu\text{m}^2$. Moreover,

$$E_C = \frac{e^2}{2C_J(S)}. \tag{D3}$$

For the junction capacitance a typical dependence on the surface area would be $C_J(S) = \alpha_C S$, with $\alpha_C = 50\,\text{fF}/\mu\text{m}^2$. The estimates used here also allow us to exemplify in Fig. 8 a possible choice for junction surface areas for the dimerized configuration necessary for the Su-Schrieffer-Heeger model. This choice is governed by the requirement that the spread in the tunnel rates preserves the dimerization, in accordance with our analysis of bond disorders. We conclude that, for typical junction parameters like those chosen here, it is possible, in principle, to realize a dimerized configuration, even at a 10% tolerance for the junction surface areas.

For completeness, we now study the effects of disorder on the spectrum of the Su-Schrieffer-Heeger Hamiltonian. We consider the following tight-binding model:

$$h^- = \sum_{i=0}^{N-1} W_{\text{site},i}|i\rangle\langle i| - \sum_{i=0}^{N-2}(t_i + W_{\text{bond},i})|i\rangle\langle i+1| + \text{H.c.,}$$

$$\tag{D4}$$

where we implement the dimerization by setting

$$t_0 = t_2 = \cdots = 0.5\Delta, \quad t_1 = t_3 = \cdots = \Delta, \tag{D5}$$

where Δ is the band gap. Moreover, Eq. (D4) generalizes Eq. (8) of the main text with the introduction of on-site disorders $W_{\text{site},i}$ uniformly distributed in the interval $[-\frac{W_{\text{site}}}{2}, \frac{W_{\text{site}}}{2}]$ and tunnel term disorder $W_{\text{bond},i}$ uniformly distributed in $[-\frac{W_{\text{bond}}}{2}, \frac{W_{\text{bond}}}{2}]$ for all i running over the ranges in Eq. (D4).

For both bond disorder [Fig. 9(a)] and on-site disorder [Fig. 9(b)] we diagonalize numerically Eq. (D4) with 30 sites and variable disorder strength and show the spectrum. We perform diagonalizations for an ensemble of 1000 disordered systems. We find that the degeneracy of the boundary states is preserved up to strong bond disorder W_{bond} on the order of the band gap Δ (equivalently, the degeneracy is preserved for bond disorder that preserves the dimerization of the hopping rates). On the other hand, the degeneracy of the boundary states is immediately split by on-site disorder W_{site}, and the splitting is proportional to W_{site}.
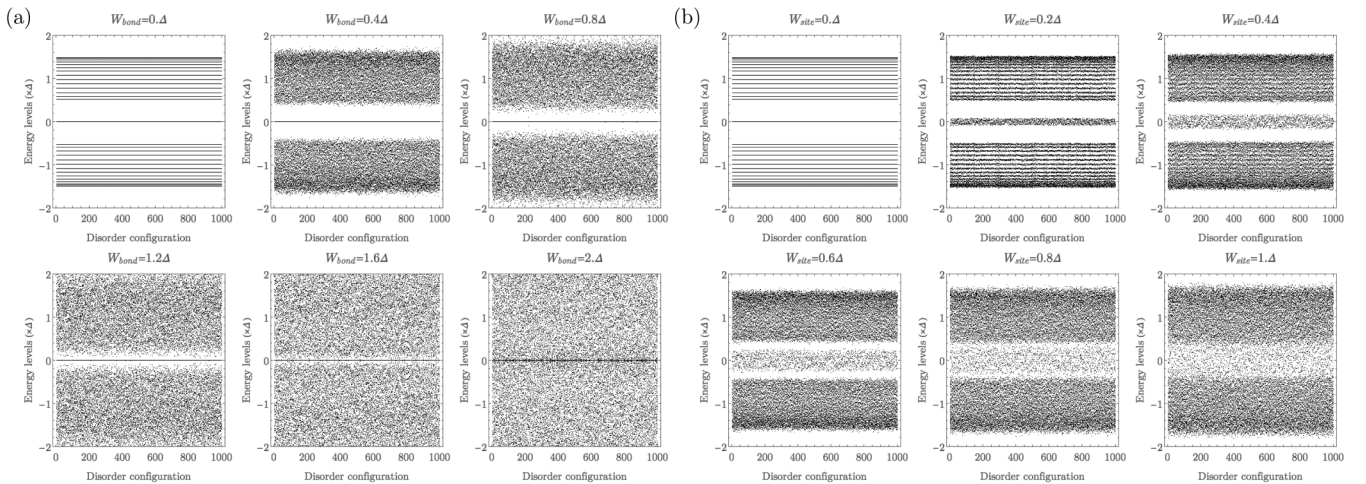

FIG. 9. (a) Effect of increasing bond disorder W_{bond} on the spectrum of the Su-Schrieffer-Heeger model with open boundary conditions. The degenerate boundary states subsist up to strong disorder (the size of the gap). (b) On-site disorder W_{site} splits the degeneracy of the boundary states, on average by an amount equal to W_{site}.

[1] A. Blais, R.-S. Huang, A. Wallraff, S. M. Girvin, and R. J. Schoelkopf, Phys. Rev. A **69**, 062320 (2004).

[2] A. Blais, J. Gambetta, A. Wallraff, D. I. Schuster, S. M. Girvin, M. H. Devoret, and R. J. Schoelkopf, Phys. Rev. A **75**, 032329 (2007).

[3] J. Q. You and F. Nori, Nature (London) **474**, 589 (2011).

[4] I. Bloch, J. Dalibard, and S. Nascimbéne, Nat. Phys. **8**, 267 (2012).

[5] M. Johanning, A. F. Varón, and C. Wunderlich, J. Phys. B **42**, 154009 (2009).

[6] R. Blatt and C. F. Roos, Nat. Phys. **8**, 277 (2012).

[7] R. Fazio and H. van der Zant, Phys. Rep. **355**, 235 (2001).

[8] I. M. Georgescu, S. Ashhab, and F. Nori, Rev. Mod. Phys. **86**, 153 (2014).

[9] M. P. A. Fisher, P. B. Weichman, G. Grinstein, and D. S. Fisher, Phys. Rev. B **40**, 546 (1989).

[10] M. J. Hartmann, F. G. S. L. Brandão, and M. B. Plenio, Nat. Phys. **2**, 849 (2006).

[11] D. G. Angelakis, M. F. Santos, and S. Bose, Phys. Rev. A **76**, 031805 (2007).

[12] M. J. Hartmann, F. G. S. L. Brandao, and M. B. Plenio, Laser Photonics Rev. **2**, 527 (2008).

[13] M. I. Makin, J. H. Cole, C. Tahan, L. C. L. Hollenberg, and A. D. Greentree, Phys. Rev. A **77**, 053819 (2008).

[14] J. Koch and K. Le Hur, Phys. Rev. A **80**, 023811 (2009).

[15] A. A. Houck, H. E. Türeci, and J. Koch, Nat. Phys. **8**, 292 (2012).

[16] M. Schiró, M. Bordyuh, B. Öztop, and H. E. Türeci, Phys. Rev. Lett. **109**, 053601 (2012).

[17] S. Schmidt and J. Koch, Ann. Phys. (Berlin, Ger.) **525**, 395 (2013).

[18] J.-M. Reiner, M. Marthaler, J. Braumüller, M. Weides, and G. Schön, Phys. Rev. A **94**, 032338 (2016).

[19] J. Cho, D. G. Angelakis, and S. Bose, Phys. Rev. Lett. **101**, 246809 (2008).

[20] A. L. C. Hayward, A. M. Martin, and A. D. Greentree, Phys. Rev. Lett. **108**, 223602 (2012).

[21] M. Fitzpatrick, N. M. Sundaresan, A. C. Y. Li, J. Koch, and A. A. Houck, Phys. Rev. X **7**, 011016 (2017).

[22] P. J. J. O'Malley, R. Babbush, I. D. Kivlichan, J. Romero, J. R. McClean, R. Barends, J. Kelly, P. Roushan, A. Tranter, N. Ding, B. Campbell, Y. Chen, Z. Chen, B. Chiaro, A. Dunsworth, A. G. Fowler, E. Jeffrey, E. Lucero, A. Megrant, J. Y. Mutus, M. Neeley, C. Neill, C. Quintana, D. Sank, A. Vainsencher, J. Wenner, T. C. White, P. V. Coveney, P. J. Love, H. Neven, A. Aspuru-Guzik, and J. M. Martinis, Phys. Rev. X **6**, 031007 (2016).

[23] R. Barends, L. Lamata, J. Kelly, L. García-Álvarez, A. G. Fowler, A. Megrant, E. Jeffrey, T. C. White, D. Sank, J. Y. Mutus, B. Campbell, Y. Chen, Z. Chen, B. Chiaro, A. Dunsworth, I.-C. Hoi, C. Neill, P. J. J. O'Malley, C. Quintana, P. Roushan, A. Vainsencher, J. Wenner, E. Solano, and J. M. Martinis, Nat. Commun. **6**, 7654 (2015).

[24] T. Niemczyk, F. Deppe, H. Huebl, E. P. Menzel, F. Hocke, M. J. Schwarz, J. J. Garcia-Ripoll, D. Zueco, T. Hümmer, E. Solano, A. Marx, and R. Gross, Nat. Phys. **6**, 772 (2010).

[25] F. Yoshihara, T. Fuse, S. Ashhab, K. Kakuyanagi, S. Saito, and K. Semba, Nat. Phys. **13**, 44 (2017).

[26] P. Forn-Díaz, J. J. García-Ripoll, B. Peropadre, J.-L. Orgiazzi, M. A. Yurtalan, R. Belyansky, C. M. Wilson, and A. Lupascu, Nat. Phys. **13**, 39 (2017).

[27] J. Braumüller, M. Marthaler, A. Schneider, A. Stehli, H. Rotzinger, M. Weides, and A. V. Ustinov, Nat. Commun. **8**, 779 (2017).

[28] N. K. Langford, R. Sagastizabal, M. Kounalakis, C. Dickel, A. Bruno, F. Luthi, D. J. Thoen, A. Endo, and L. DiCarlo, Nat. Commun. **8**, 1715 (2017).

[29] K. Le Hur, L. Henriet, A. Petrescu, K. Plekhanov, G. Roux, and M. Schiró, C. R. Phys. **17**, 808 (2016).

[30] K. W. Murch, U. Vool, D. Zhou, S. J. Weber, S. M. Girvin, and I. Siddiqi, Phys. Rev. Lett. **109**, 183602 (2012).

[31] Z. Leghtas, S. Touzard, I. M. Pop, A. Kou, B. Vlastakis, A. Petrenko, K. M. Sliwa, A. Narla, S. Shankar, M. J. Hatridge, M. Reagor, L. Frunzio, R. J. Schoelkopf, M. Mirrahimi, and M. H. Devoret, Science **347**, 853 (2015).

[32] M. E. Kimchi-Schwartz, L. Martin, E. Flurin, C. Aron, M. Kulkarni, H. E. Tureci, and I. Siddiqi, Phys. Rev. Lett. **116**, 240503 (2016).

[33] C. Aron, M. Kulkarni, and H. E. Türeci, Phys. Rev. A **90**, 062305 (2014).

[34] C. Aron, M. Kulkarni, and H. E. Türeci, Phys. Rev. X **6**, 011032 (2016).

[35] N. A. Masluk, I. M. Pop, A. Kamal, Z. K. Minev, and M. H. Devoret, Phys. Rev. Lett. **109**, 137002 (2012).

[36] K. K. Likharev and V. K. Semenov, IEEE Trans. Appl. Supercond. **1**, 3 (1991).

[37] O. A. Mukhanov, IEEE Trans. Appl. Supercond. **21**, 760 (2011).

[38] K. G. Fedorov, A. V. Shcherbakova, M. J. Wolf, D. Beckmann, and A. V. Ustinov, Phys. Rev. Lett. **112**, 160502 (2014).

[39] A. Wallraff, A. Lukashenko, J. Lisenfeld, A. Kemp, M. V. Fistul, Y. Koval, and A. V. Ustinov, Nature (London) **425**, 155 (2003).

[40] J. E. Mooij and C. J. P. M. Harmans, New J. Phys. **7**, 219 (2005); O. V. Astafiev, L. B. Ioffe, S. Kafanov, Y. A. Pashkin, K. Y. Arutyunov, D. Shahar, O. Cohen, and J. S. Tsai, Nature (London) **484**, 355 (2012).

[41] A. Belkin, M. Belkin, V. Vakaryuk, S. Khlebnikov, and A. Bezryadin, Phys. Rev. X **5**, 021023 (2015).

[42] M. T. Bell, W. Zhang, L. B. Ioffe, and M. E. Gershenson, Phys. Rev. Lett. **116**, 107002 (2016).

[43] V. E. Manucharyan, J. Koch, L. I. Glazman, and M. H. Devoret, Science **326**, 113 (2009).

[44] M. T. Bell, I. A. Sadovskyy, L. B. Ioffe, A. Y. Kitaev, and M. E. Gershenson, Phys. Rev. Lett. **109**, 137003 (2012).

[45] H. Meier, R. T. Brierley, A. Kou, S. M. Girvin, and L. I. Glazman, Phys. Rev. B **92**, 064516 (2015).

[46] A. Kou, W. C. Smith, U. Vool, R. T. Brierley, H. Meier, L. Frunzio, S. M. Girvin, L. I. Glazman, and M. H. Devoret, Phys. Rev. X **7**, 031037 (2017).

[47] S. Backens, A. Shnirman, Y. Makhlin, Y. Gefen, J. E. Mooij, and G. Schön, Phys. Rev. B **96**, 195402 (2017).

[48] L. Grünhaupt, N. Maleeva, S. T. Skacel, M. Calvo, F. Levy-Bertrand, A. V. Ustinov, H. Rotzinger, A. Monfardini, G. Catelani, and I. M. Pop, Phys. Rev. Lett. **121**, 117001 (2018).

[49] N. Maleeva, L. Grünhaupt, T. Klein, F. Levy-Bertrand, O. Dupré, M. Calvo, F. Valenti, P. Winkel, F. Friedrich, W.

Wernsdorfer, A. V. Ustinov, H. Rotzinger, A. Monfardini, M. V. Fistul, and I. M. Pop, Nat. Commun. **9**, 3889 (2018).

[50] M. Kardar, Phys. Rev. B **33**, 3125 (1986).

[51] G. E. Santoro and E. Tosatti, J. Phys. A **39**, R393 (2006).

[52] S. Coleman, *Aspects of Symmetry* (Cambridge University Press, Cambridge, 1988).

[53] A. I. Vainshtein, V. I. Zakharov, V. A. Novikov, and M. A. Shifman, Sov. Phys. Usp. **25**, 195 (1982).

[54] K. A. Matveev, A. I. Larkin, and L. I. Glazman, Phys. Rev. Lett. **89**, 096802 (2002).

[55] J. Koch, T. M. Yu, J. Gambetta, A. A. Houck, D. I. Schuster, J. Majer, A. Blais, M. H. Devoret, S. M. Girvin, and R. J. Schoelkopf, Phys. Rev. A **76**, 042319 (2007).

[56] E. Orignac and T. Giamarchi, Phys. Rev. B **64**, 144515 (2001).

[57] A. Petrescu and K. Le Hur, Phys. Rev. Lett. **111**, 150601 (2013).

[58] M. Piraud, F. Heidrich-Meisner, I. P. McCulloch, S. Greschner, T. Vekua, and U. Schollwöck, Phys. Rev. B **91**, 140406 (2015).

[59] A. Petrescu, M. Piraud, G. Roux, I. P. McCulloch, and K. Le Hur, Phys. Rev. B **96**, 014524 (2017).

[60] J. M. Dempster, B. Fu, D. G. Ferguson, D. I. Schuster, and J. Koch, Phys. Rev. B **90**, 094518 (2014).

[61] W. P. Su, J. R. Schrieffer, and A. J. Heeger, Phys. Rev. Lett. **42**, 1698 (1979).

[62] W. P. Su, J. R. Schrieffer, and A. J. Heeger, Phys. Rev. B **22**, 2099 (1980).

[63] S. Ryu and Y. Hatsugai, Phys. Rev. Lett. **89**, 077002 (2002).

[64] X.-G. Wen, Phys. Rev. B **85**, 085103 (2012).

[65] A. Bernevig and T. Neupert, arXiv:1506.05805.

[66] R. Jackiw and C. Rebbi, Phys. Rev. D **13**, 3398 (1976).

[67] W. P. Su and J. R. Schrieffer, Phys. Rev. Lett. **46**, 738 (1981).

[68] A. Y. Kitaev, Ann. Phys. (NY) **303**, 2 (2003).

[69] B. Douçot and J. Vidal, Phys. Rev. Lett. **88**, 227005 (2002).

[70] L. B. Ioffe and M. V. Feigel'man, Phys. Rev. B **66**, 224503 (2002).

[71] A. Kitaev, arXiv:cond-mat/0609441.

[72] S. Gladchenko, D. Olaya, E. Dupont-Ferrier, B. Douçot, L. B. Ioffe, and M. E. Gershenson, Nat. Phys. **5**, 48 (2009).

[73] P. Brooks, A. Kitaev, and J. Preskill, Phys. Rev. A **87**, 052306 (2013).

[74] W. C. Smith, A. Kou, U. Vool, I. M. Pop, L. Frunzio, R. J. Schoelkopf, and M. H. Devoret, Phys. Rev. B **94**, 144507 (2016).

[75] Y. Chu, C. Axline, C. Wang, T. Brecht, Y. Y. Gao, L. Frunzio, and R. J. Schoelkopf, Appl. Phys. Lett. **109**, 112601 (2016).

[76] J. Zak, Phys. Rev. Lett. **62**, 2747 (1989).

[77] T. Goren, K. Plekhanov, F. Appas, and K. Le Hur, Phys. Rev. B **97**, 041106(R) (2018).

[78] D. V. Averin, K. Rabenstein, and V. K. Semenov, Phys. Rev. B **73**, 094504 (2006).

[79] Q. Deng and D. V. Averin, J. Exp. Theor. Phys. **119**, 1152 (2014).

[80] C. Müller, S. Guan, N. Vogt, J. H. Cole, and T. M. Stace, Phys. Rev. Lett. **120**, 213602 (2018).

[81] J. E. Zimmerman and A. H. Silver, Phys. Rev. **141**, 367 (1966).

[82] A. H. Silver and J. E. Zimmerman, Phys. Rev. **157**, 317 (1967).

[83] D. J. Thouless, *Topological Quantum Numbers in Nonrelativistic Physics* (World Scientific, Singapore, 1998).

[84] M. Devoret, in *Les Houches, Session LXIII, 1995*, edited by S. Reynaud, E. Giacobino, and J. Zinn-Justin (Elsevier, Amsterdam, 1997), p. 351.

[85] U. Vool and M. Devoret, Int. J. Circuit Theory Appl. **45**, 897 (2017).

[86] M. Tinkham, *Introduction to Superconductivity*, 2nd ed. (McGraw-Hill, New York, 1996).

[87] V. Ambegaokar and A. Baratoff, Phys. Rev. Lett. **10**, 486 (1963); **11**, 104 (1963).